

Temperature dependence of the magnon-phonon coupling in yttrium iron garnet/gadolinium gallium garnet high overtone bulk acoustic resonators

J. Weber,^{1,2, a)} M. Müller,^{1,2, b)} M. Cherkasskii,³ S. Geprägs,¹ R. Gross,^{1,2,4} C.H. Back,^{2,4,5} S.T.B. Goennenwein,⁶ S. Viola Kusminskiy,^{3,7} M. Althammer,^{1,2} and H. Huebl^{1,2,4, c)}

¹⁾ *Walther-Meißner-Institut, Bayerische Akademie der Wissenschaften, 85748 Garching, Germany*

²⁾ *Technical University of Munich, TUM School of Natural Sciences, Physics Department, 85748 Garching, Germany*

³⁾ *Institute for Theoretical Solid State Physics, RWTH Aachen University, 52074 Aachen, Germany*

⁴⁾ *Munich Center for Quantum Science and Technology (MCQST), 80799 Munich, Germany*

⁵⁾ *Centre for Quantum Engineering (ZQE), Technical University of Munich, 85748 Garching, Germany*

⁶⁾ *Department of Physics, University of Konstanz, 78457 Konstanz, Germany*

⁷⁾ *Max Planck Institute for the Science of Light, 91058 Erlangen, Germany*

We experimentally study the temperature dependence of the magnon-phonon coupling in a yttrium iron garnet (YIG)/gadolinium gallium garnet (GGG) heterostructure. More specifically, we use broadband ferromagnetic resonance to investigate the magneto-elastic coupling between the Kittel mode of a YIG thin film and the transverse acoustic phonon modes of the YIG/GGG high overtone bulk acoustic wave acoustic resonator for in and out-of-plane field directions in the temperature range between $T = 5$ K and 300 K. We find that for a magnetic field applied normal to the film surface, magneto-elastic coupling decreases with decreasing temperature, whereas it increases for the in-plane magnetic field configuration. The observed temperature dependence differs from earlier observations on bulk YIG samples, which might be due to the temperature dependent stress imposed by the GGG substrate.

I. INTRODUCTION

The coupling between spin and lattice degrees of freedom is of fundamental importance to magnetic materials. It allows to excite magnetization dynamics [1–11], affects the damping properties of the magnetization dynamics [12–17], enables the control of the magnetization direction [1, 2, 18–24], and allows to create perpendicular magnetic anisotropy [1, 25–28]. The spin-lattice coupling concomitantly results in a finite interaction of the associated elementary excitations, i.e., magnons and phonons, giving rise to the formation of hybridized modes [7, 29–32]. Recently, the resonant interaction of magnons and phonons mediated by magneto-elastic coupling regained interest in the context of understanding magnetization damping, excitation of helical phonons, strong coupling phenomena, as well as applications in quantum sensing and transduction [10, 11, 33–51]. In this context, many experiments explore bulk acoustic wave (BAW) resonators based on gadolinium gallium garnet ($\text{Gd}_3\text{Ga}_5\text{O}_{12}$, GGG) substrates combined with a layer of ferrimagnetic yttrium iron garnet ($\text{Y}_3\text{Fe}_5\text{O}_{12}$, YIG) [35–37], mostly due to the exceptional damping properties of YIG [52–55]. However, the majority of experiments so far have focused

on room-temperature properties, because the magnetization damping of YIG increases at cryogenic temperatures [52, 53, 56, 57]. At the same time, the acoustic losses [58–61] are strongly reduced at low temperatures what could result in overall improved cooperativities C . The magneto-elastic coupling in YIG is also temperature dependent, and, moreover, anisotropic, since the interaction reflects the symmetry of the lattice [62–64]. Hence, the precise temperature dependence of the magnetoelastic interaction in garnet-based heterostructures is of great interest for magneto-acoustic hybrids for low-temperature and potential quantum applications [46, 47].

Here, we explore the coupling between the magnetic excitations of YIG and the elastic excitations of bulk acoustic resonator modes of the YIG/GGG heterostructure system between 5 K and room temperature. Using broadband ferromagnetic resonance spectroscopy, we extract the magneto-elastic coupling strength and anisotropy, as well as the magnetic and acoustic damping rates. We find that the damping of the magnetization dynamics due to magneto-elastic coupling is strongly temperature-dependent and anisotropic.

II. EXPERIMENTAL DETAILS

In our experiments, we studied a BAW resonator comprised of a $d = 220$ nm thick, (111) YIG film grown via liquid phase epitaxy (LPE) on a crystalline GGG substrate with a thickness of $L = 530$ μm . As sketched in Fig. 1, the sample is mounted face-down onto a copla-

^{a)}Electronic mail: johannes.weber@wmi.badw.de; Contributed equally to this work

^{b)}Contributed equally to this work

^{c)}Electronic mail: huebl@wmi.badw.de

nar waveguide (CPW), which is connected to a vector network analyzer (see Ref. [60, 61] for details). We perform temperature-dependent broadband ferromagnetic resonance experiments (bbFMR), i.e., we measure the complex transmission parameter S_{21} as a function of frequency and applied magnetic field H_{ext} for various sample temperatures ranging from 5 K to room temperature [65]. To this end, the sample with the CPW is mounted in the variable-temperature insert of a liquid helium cryostat. The external magnetic field is applied either parallel to the surface normal and perpendicular to the transmission line of the CPW (out-of-plane, oop) or perpendicular to both the surface normal and the transmission line of the CPW (in-plane, ip) (see Fig. 1 (a) and (b)).

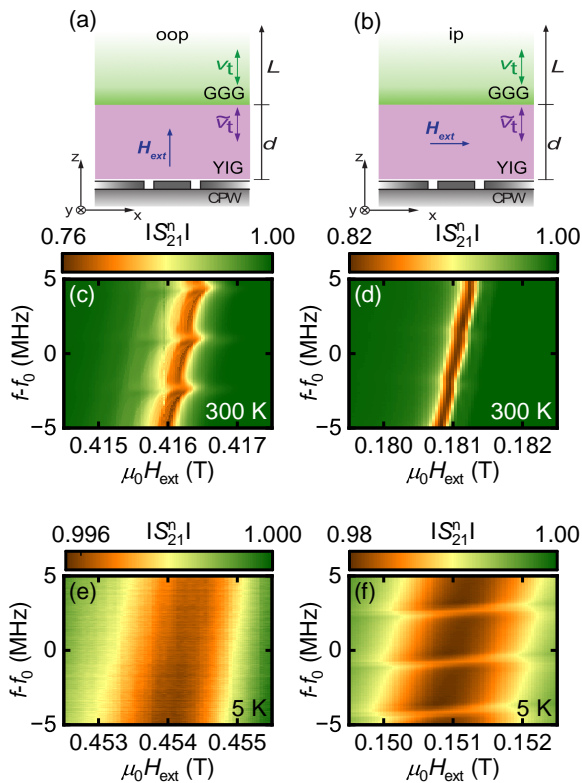


Figure 1. (a),(b) Coordinate system as well as schematic of the sample composed of a ferrimagnetic YIG thin film with a thickness d on a GGG substrate with thickness L , mounted on a coplanar waveguide (CPW). The external magnetic field H_{ext} is either applied out of the thin film plane (oop) along the z -direction (panels (a), (c), (e)) or in-plane (ip) along the x -direction (panels (b), (d), (f)). The two different sound velocities are referred to as \tilde{v}_t (YIG) and v_t (GGG). Panels (c)-(f) show the normalized complex transmission amplitude $|S_{21}^n|$ as a function of the external magnetic field H_{ext} and the microwave frequency $f - f_0$ with $f_0 = 7$ GHz for $T = 300$ K and 5 K as well as for the ip and oop magnetic field configuration.

Figure 1 (c)-(f) displays the broadband ferromagnetic resonance data in form of the normalized absolute trans-

mission amplitude $|S_{21}^n| = |S_{21}/S_{21}^0|$, with S_{21}^0 as a cut at constant field off-resonant of the Kittel mode, as a function of the microwave frequency $f - f_0$ with $f_0 = 7$ GHz and the applied magnetic field $\mu_0|\mathbf{H}_{\text{ext}}|$ for \mathbf{H}_{ext} along the z -direction (oop, see panel (c), (e)) and x -direction (ip, see panel (d), (f)) for $T = 5$ K and 300 K, respectively [66]. This high-resolution zoom into the broadband microwave absorption data shows the Kittel mode as an absorption signature in brown color. The linear relation between the resonance frequency and the applied magnetic field originates from the gyromagnetic ratio of YIG. The magnetic field range of panel (c)-(f) is 3 mT, however, the center field varies due to the impact of the shape anisotropy and the change of the saturation magnetization with temperature [67]. As evident from Fig. 1, we find additional absorption signatures which are periodic in frequency, indicating the coupling of the Kittel mode to the resonant elastic excitations of the bulk acoustic wave resonator. Their frequency separation or free spectral range (FSR) of $f_{\text{FSR}} = 3.57$ MHz at 5 K is related to the shear wave velocities of the elastic excitations and thickness of the total layer stack via $f_{\text{FSR}} = 1/(2(d/\tilde{v}_t + L/v_t))$ [34]. Here, $d = 220$ nm and $\tilde{v}_t = 3843$ ms $^{-1}$ [34] are the thickness and the transverse acoustic sound velocity of the YIG thin film, and $L = 530$ μm and $v_t = 3568$ ms $^{-1}$ [34] are the thickness and transverse acoustic sound velocity of the GGG substrate. As $L \gg d$, the acoustic properties of the layer stack are dominated by the elastic properties of GGG. Therefore, we find good agreement of the measured FSR with the calculated one using the elastic properties of GGG. By analyzing the FMR linewidth at a frequency off-resonant with the acoustic modes, we determine the change of linewidth with temperature. The FMR linewidth clearly increases at low temperatures in agreement with literature [34, 52, 54, 68] (see also Fig. 3).

In addition, we find a remarkable difference in the visibility of the frequency-periodic features due to magneto-elastic coupling for experiments with in-plane and out-of-plane field direction. At $T = 300$ K,

we observe a clear signature of magnon-phonon coupling for the out-of-plane magnetic field configuration in agreement with the room-temperature results in Ref. [42], while such a signature is absent at $T = 5$ K. The opposite is the case for the in-plane magnetic field configuration. Since the visibility of this signature depends on the magneto-elastic coupling strength, the data in Fig. 1 suggest that the anisotropy of the magneto-elastic interaction and the magnitude of its components change as a function of temperature.

III. MODELING OF MAGNON-PHONON COUPLING AND COMPARISON WITH DATA

In order to understand the interaction between the magnetic excitations confined to the thin YIG film and the elastic excitations extending over the entire sample

stack comprised of the YIG film and the GGG substrate, several factors have to be considered. In particular, one has to take into account the acoustic mode matching, the elastic coupling at the interface, the mode matching between the relevant acoustic and magnetic modes, the details of the sample geometry, as well as the material parameters describing the magnetization dynamics in the thin film, the acoustic excitations in the layer stack, and the magneto-elastic coupling giving rise to the magnon-phonon coupling [33, 34, 69–71]. For the quantitative analysis of the relevant parameters, we employ the models developed in [34, 69]. In our experimental situation, the normal on the YIG/GGG bilayer is oriented approximately along the [111] direction of YIG. Furthermore, we need to account for deviations in the phonon propagation with respect to the crystallographic [111]-direction, originating e.g. from a finite miscut of the GGG substrate [60]. We fit our data to the description presented in Ref. [69], which accounts for those details. In Appendix B, we extend this approach to account for in-plane magnetic fields. Thereby, we relate the Polder susceptibility to the experimentally measured data using [72]

$$S_{21}(f, H_{\text{ext}}) = A + DH_{\text{ext}} + \sum_n^N E e^{i\phi} \chi_n(f, H_{\text{ext}}). \quad (1)$$

Here, A and D are parameters that account for a complex background of the microwave transmission up to linear order in the applied external magnetic field H_{ext} . In addition, E is the coupling between the sample and the magnetic circuit [73] and ϕ corrects phase shifts, which originate from the experimental setup. Equation (1) allows us to quantitatively analyze our data. In particular, we perform a least mean square 2D-fit of the complex transmission data recorded as function of the frequency and the applied magnetic field for all temperatures, which allows us to determine the parameters associated with the microwave detection setup (A , D , E and ϕ) as well as the Polder susceptibility providing insights into the magnetization dynamics, the coupling to the elastic excitations of the acoustic resonator, as well as the acoustic damping.

A. Comparison of model predictions and data

Figure 2 compares the experimental data with the fit result. This asserts the adequacy of the fit model, which reproduces the experimental data with high accuracy. The susceptibility derived in Refs. [34, 69] and explicitly stated for our analysis in App. B is used for the fitting and depends on multiple parameters. Practically, we optimize the effective magnetization $M_{\text{eff}}^{\text{ip,oop}}$, the magnetic damping rate κ_s , the acoustic damping rate η_a and the magneto-elastic coupling parameter $B_{\text{ip/oop}}$. The following parameters are fixed: (i) the transverse phonon propagation velocities $v_t^{x,y} = 3568$ m/s which are degenerate for a propagation along the [111]-direction in GGG [74],

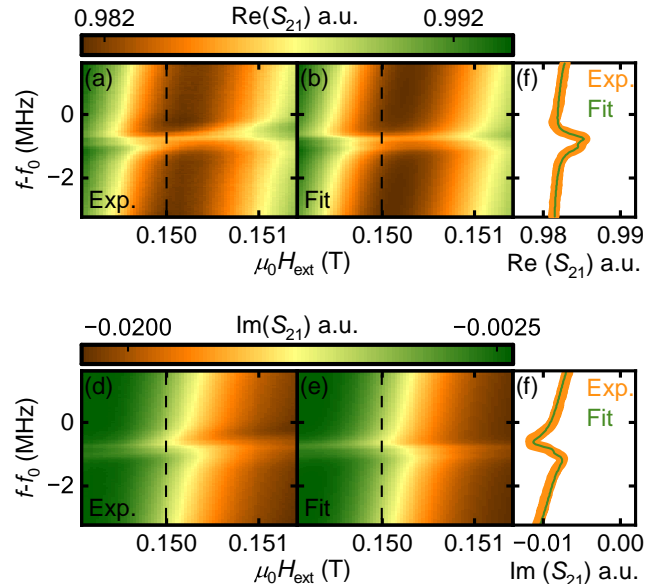


Figure 2. Panels (a) and (d) show the real and imaginary part of the transmission parameter S_{21} of a FMR measurement at 5K with the magnetic field applied within the plane of the YIG thin film. The avoided crossing with the transverse acoustic phonon mode is clearly visible as a horizontal line in the middle of the panels. Panels (b) and (e) display the result of a simultaneous 2D fit of the real and imaginary parts. Panels (c) and (f) show two exemplary line cuts at 0.1496 T represented by the black dashed vertical lines in the color plots. The orange line is the measured data, and the green line is the fit data.

(ii) the mass density $\rho = 7070$ kg/m³ [34], (iii) the shear modulus $C_{44} = 90.8$ GPa [75], and (iv) the thickness L of the GGG substrate. For the YIG layer, we fix (i) the transverse acoustic sound velocity $v_t = 3843$ m/s (ii) the mass density $\tilde{\rho} = 5170$ kg/m³, (iii) the shear modulus $\tilde{C}_{44} = 76.35$ GPa [71] and (iv) the thickness d of the YIG thin film. In addition, we assume that the acoustic damping is identical for GGG and YIG $\eta_a = \tilde{\eta}_a$. Last but not least, the susceptibility also includes the gyromagnetic ratio, which is determined independently and set to $\gamma/2\pi = 28$ GHz/T.

The exact elastic resonance frequencies of the bulk acoustic resonator are temperature dependent due to the thermal expansion of the layer stack and subtle changes in the elastic parameters of the material [61]. We account for this in our fit by introducing an artificial frequency offset Δf that corrects the resonance frequency of the transverse acoustic phonon modes to match the frequencies observed in experiment.

Additionally, we have four (complex) fit parameters that account for A , D , E , and ϕ in Eq. (1), which are approximately temperature independent.

Figure 2 (a) and (d) present the real and imaginary part of the transmission parameter S_{21} of a bbFMR mea-

surement at 5 K in the ip magnetic field configuration. The data are zoomed in on a single avoided crossing between the two transverse acoustic phonon modes and the Kittel mode. Panels (b) and (e) show the corresponding fit of Eq. (1) to the experimental data, while panels (c) and (f) display an exemplary cut at $\mu_0 H_{\text{ext}} = 0.1496$ T, (see black dashed lines in panels (a), (b), (d) and (e)). The measurement data, represented by the orange lines in panels (c) and (f), agree well with the fit presented as a green line. Furthermore, the real and imaginary parts of the transmission parameter S_{21} agree quantitatively with our theoretical model. In addition to the data presented in Fig. 1, we analyze further experimental data recorded for temperatures between $T = 5$ K and 300 K using this procedure for magnetic fields aligned along the normal and in-plane direction of the sample. The extracted parameters are discussed in the following.

B. Temperature dependence of material parameters

We next discuss the temperature dependence of the material parameters obtained from fitting the experimental data. Figure 3 (a) and (b) show the temperature dependence of the magnetic and acoustic damping rates, κ_s and η_a , respectively, for the ip (blue open circles) and oop (red open circles) magnetic field configuration. Here, the magnetic damping rate does not include the damping originating from the coupling to the elastic excitations of the BAW resonator. The magnetic damping κ_s continuously increases towards lower temperatures. Note that we measured and evaluated the data for the oop magnetic field configuration down to 70 K, where a coupling between the magnetic and elastic subsystems still can be resolved in our experiments. The damping rate for the oop configuration at 5 K is extracted by fitting a Polder susceptibility without coupling to the elastic excitations [76]. For the ip magnetic field configuration, we find a monotonic increase from $T = 300$ K to 30 K followed by a plateau for even lower temperatures. This observation is commonly reported for YIG and attributed to the coupling of the magnetization dynamics to impurities [52, 54, 77]. Panel (b) shows the expected monotonic increase of the acoustic damping rate η_a measured at $f_0 = 7$ GHz with increasing temperature. This can be attributed to the scattering of the excited transverse acoustic phonons with thermal phonons [59, 78]. Our data suggests that both the acoustic and magnetic relaxation behaviors are independent of the measurement geometry (ip or oop), which can be understood in the sense that they represent bulk properties of the magnetic and acoustic subsystem.

In addition to the relaxation rates, we extract the magneto-elastic coupling constants B_{oop} and B_{ip} by fitting the data (see Fig. 3 (c)). These constants are linked to the magneto-elastic coupling constants of the crystalline systems via $B_{\text{oop}} = (2B_1 + B_2)/3$ and $B_{\text{ip}} = \sqrt{2}(B_2 - B_1)/3$, respectively [79]. The latter are related

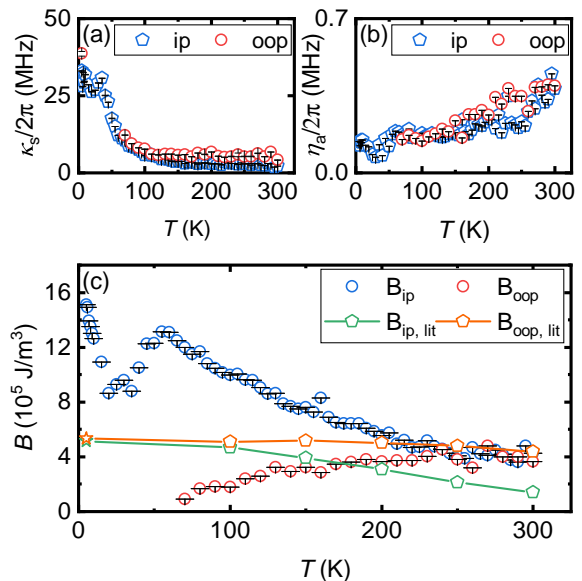


Figure 3. Magnetic κ_s (a) and acoustic η_a (b) damping rates of the YIG/GGG high overtone bulk acoustic wave resonator as a function of temperature for both the ip and oop magnetic field configuration. Panel (c) shows the temperature dependence of the coupling parameters B_{ip} and B_{oop} (blue and red circles, respectively) obtained from fitting the experimental data. Also shown are $B_{\text{ip, lit}}$ and $B_{\text{oop, lit}}$ derived from literature data on bulk YIG. The two stars mark the extrapolated values at 5 K. The error bars originate from the covariance matrix of the least mean square fit.

to the magnetostriction constants of a cubic system via $\lambda_{100} = -\frac{2}{3} \frac{B_1}{C_{11} - C_{12}}$ and $\lambda_{111} = -\frac{B_2}{3C_{44}}$ (cf. Ref. [80]). Figure 3 (c) also includes data for bulk YIG from Cullen *et al.* [62, 63] obtained from the published temperature-dependent magnetostriction parameters λ_{100} and λ_{111} for the temperature range between 100 K and 300 K. For the oop magnetic field configuration, we find reasonable quantitative agreement within 25% with the literature values for $T \geq 150$ K. Below $T \approx 150$ K, we observe a reduction in B_{oop} down to a level, where our fit is compatible with $B_{\text{oop}} = 0$. For the ip field orientation, we determine a similar temperature dependence compared to Refs. [62, 63], however, our magneto-elastic parameter is approximately a factor of 2 larger. Moreover, between 5 K and 100 K, we observe an additional increase of B_{ip} up to $13.12 \times 10^5 \frac{\text{J}}{\text{m}^3}$. Note that the data by Cullen *et al.* [62] extrapolates the magneto-elastic constant in this temperature regime using the theory of magnetostriction in a cubic insulator applied to a ferrimagnet and using the sublattice magnetization data of C. Robert [81]. Interestingly, while our data is in rough agreement with the observations for bulk YIG for elevated temperatures, we find discrepancies for lower T . We attribute this to the different growth techniques employed. Our 220 nm thick YIG film is grown using liquid-phase epitaxy tech-

niques, which involve solvents such as lead and boron oxides, potentially leading to a residual contamination of the magnetic film. In addition, we expect a difference in the expansion coefficient between YIG and GGG, resulting in additional strain at lower temperatures. Together, these aspects could explain the difference in the observed magneto-elastic coupling coefficient.

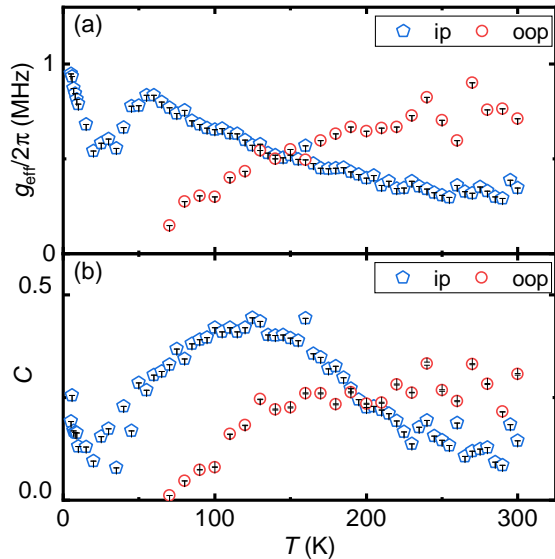


Figure 4. (a) Effective coupling strength g_{eff} as a function of temperature calculated from Eqs. (2), (3) for the ip (blue) and oop (red) magnetic field geometry. (b) Cooperativity $C = g_{\text{eff}}^2/\eta_a\kappa_s$ as a function of temperature for both geometries. The error bars originate from the covariance matrix of the least mean square fit.

We next discuss the magnon-phonon coupling rate in the context of magnon-phonon hybrids. The magneto-elastic coupling constant $B_{\text{ip}/\text{oop}}$ is linked to the magneto-elastic coupling rate g_{eff} via [35, 42, 82]

$$g_{\text{eff,ip}}(f) = \frac{B_{\text{ip}}}{2} \sqrt{\frac{g^2 \mu_B^2 \mu_0 H_{\text{res,ip}}}{h^2 f^2 M_s \tilde{\rho}_t d (L+d)}} \left[1 - \cos\left(2\pi \frac{fd}{\tilde{v}_t}\right) \right] \quad (2)$$

and

$$g_{\text{eff,oop}}(f) = B_{\text{oop}} \sqrt{\frac{g \mu_B}{h f M_s \tilde{\rho}_t d (L+d)}} \left[1 - \cos\left(2\pi \frac{fd}{\tilde{v}_t}\right) \right]. \quad (3)$$

Here, g is the Landé g-factor of YIG, μ_B the Bohr magneton, h the Planck constant, M_s the saturation magnetization of YIG and $\mu_0 H_{\text{res,ip}}$ the resonance field of the magnon Kittel mode at $f_0 = 7$ GHz for the in-plane configuration [83]. Using the bbFMR information about the magnetic field dependence of the magnetic resonance frequency, we determine the effective magnetization $M_{\text{eff}} = M_s - 2K_u/M_s$, which contains the saturation magnetization and contributions of the uniaxial

magnetic anisotropy. As discussed in Appendix A, we extract from this data the effective magnetization M_{eff} , which we use to calculate the effective coupling strengths in Eqs. (2), (3), instead of the saturation magnetization M_s , since the uniaxial anisotropy is typically on the order of a few mT [84] and therefore small compared to the saturation magnetization M_s .

Figure 4 (a) shows the obtained magneto-elastic coupling rate g_{eff} for both geometries. Interestingly, the coupling rate increases by a factor of three when the temperature is increased from 70 K to 300 K for magnetic fields oriented along the oop direction. In contrast, g_{eff} for the ip magnetic field geometry shows an increase with decreasing temperature, with additional features between 5 K and 45 K. Below 45 K the coupling rate decreases, reaches a minimum around 20 K and then strongly increases again down to 5 K. This minimum in the coupling rate appears at about the same temperature, where the FMR linewidth of YIG often peaks due to slowly-relaxing rare-earth impurities [52]. The coupling rate g_{eff} , together with the damping rates κ_s and η_a , allow us to quantify the temperature dependence of the cooperativity $C = g_{\text{eff}}^2/\eta_a\kappa_s$, for both field orientations (see Fig 4 (b)). For the oop magnetic field geometry, we find the maximum of C around 160 K. Below this temperature, C decreases due to enhanced magnetic damping. For the ip magnetic field configuration, the maximum is found around 105 K. The minimum of C at approximately 25 K is attributed again to the increased magnetization damping of YIG. However, below 30 K, κ_s is nearly constant, while g_{eff} still increases towards lower T resulting in an increase of C towards lower temperature.

IV. CONCLUSION

We report on the temperature dependence of the magneto-elastic interaction in yttrium iron garnet/gadolinium gallium garnet high overtone bulk acoustic resonators. The bulk acoustic wave resonator is realized as a bilayer comprising a yttrium iron garnet magnetic thin film and a single-crystalline gadolinium gallium garnet substrate. Making use of the model presented in Ref. [69], we fit our experimental data to extract the effective magneto-elastic coupling rate and the damping rates of the coupled subsystem. In particular, we determine the temperature dependence of these quantities between 5 K and 300 K. We find that the magneto-elastic constant for the ip magnetic field configuration exceeds that for the oop magnetic field configuration below 150 K, while the magnetic damping remains about constant in this temperature range. Neither the decrease for the oop magnetic field configuration nor the increase in the magneto-elastic coupling constant below $T = 100$ K for the ip magnetic field configuration is expected from the bulk literature values. Our experiments demonstrate that low-temperature experiments are conceptually feasible and enable high cooperativities and a reduced number

of thermal noise quanta. The presented results can serve as guidance for the design of magnon-phonon-based signal transduction schemes as discussed in Refs. [46, 47, 85].

ACKNOWLEDGMENTS

We acknowledge financial support by the Deutsche Forschungsgemeinschaft (DFG, German Research Foundation) via the research unit CHiPS (541503763), Germany's Excellence Strategy EXC-2111-390814868, and the Transregio ConQuMat (TRR 360 – 492547816). This research is part of the Munich Quantum Valley, which is supported by the Bavarian state government with funds from the Hightech Agenda Bayern Plus (Light-house Project NeQuS).

Appendix A: Temperature dependence of the saturation magnetization and the uniaxial anisotropy

We fit the effective magnetization $M_{\text{eff}}^{\text{ip,oop}}$ for each geometric configuration (ip, oop), respectively. From these effective magnetizations and the resonance fields, we calculate the cubic anisotropy K_1/M_s using the following Kittel equations [86–89] for the ip and oop resonance frequency of a magnetic thin film as a function of the resonance magnetic field $\mu_0 H_{\text{res}}^{\text{ip,oop}}$

$$f_{\text{res}}^{\text{oop}} = \frac{\gamma}{2\pi} \mu_0 \left(H_{\text{res}}^{\text{oop}} - M_s - \frac{4K_1}{3M_s} + \frac{2K_u}{M_s} \right), \quad (\text{A1})$$

and

$$f_{\text{res}}^{\text{ip}} = \frac{\gamma}{2\pi} \mu_0 \sqrt{H_{\text{res}}^{\text{ip}} \left(H_{\text{res}}^{\text{ip}} + M_s - \frac{K_1}{M_s} - \frac{2K_u}{M_s} \right)}, \quad (\text{A2})$$

where $M_{\text{eff}}^{\text{oop}} = M_s + \frac{4K_1}{3M_s} - \frac{2K_u}{M_s}$ and $M_{\text{eff}}^{\text{ip}} = M_s - \frac{K_1}{M_s} - \frac{2K_u}{M_s}$. The ratio K_1/M_s displayed in Fig. 5 (b) is determined via $\frac{3}{7}(M_{\text{eff}}^{\text{oop}} - M_{\text{eff}}^{\text{ip}})$.

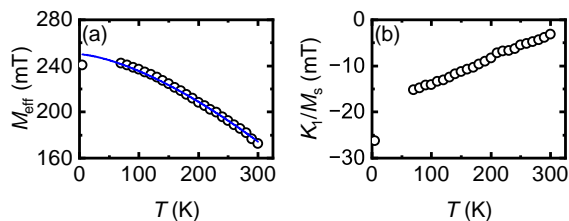


Figure 5. (a) Temperature dependence of the effective magnetization M_{eff} . The blue continuous line represents a fit to the Bloch $T^{3/2}$ law. [90] (b) Temperature dependence of the cubic anisotropy field K_1/M_s in the YIG thin film.

Fig. 5 shows the temperature dependence of an effective magnetization $M_{\text{eff}} = \mu_0 M_s - 2K_u/M_s = M_{\text{eff}}^{\text{ip}} + \frac{K_1}{M_s}$,

which is the saturation magnetization adjusted by the uniaxial anisotropy field as a function of temperature, which agrees well within 10 % with previously reported values for the saturation magnetization [91]. This leads via propagation of uncertainty to a 5 % uncertainty for the ip and oop effective coupling strengths $g_{\text{eff}}^{\text{ip,oop}}$ in Fig. 4. The blue continuous line represents a fit of the data to the Bloch $T^{3/2}$ law [90]

$$M_{\text{eff}}(T) = M_{\text{eff}}(0) \left(1 - \left(\frac{T}{T_c} \right)^{3/2} \right), \quad (\text{A3})$$

where $M_{\text{eff}}(0) = 250.1$ mT and $T_c = 665$ K is the critical temperature approximating the $T^{3/2}$ dependence in considering the investigated temperature range. We use this fit to calculate the ip and oop effective coupling strengths $g_{\text{eff}}^{\text{ip,oop}}$ shown in Fig. 4.

Appendix B: Used fitting function for the broadband ferromagnetic resonance

We consider a bilayer system in which the non-magnetic layer occupies the region $d \leq z \leq L$, while the ferromagnetic layer extends over $0 \leq z \leq d$. The magnetization dynamics in the ferromagnet is described by the Landau-Lifshitz-Gilbert (LLG) equation,

$$\partial_t \mathbf{M} = -\gamma \mu_0 \mathbf{M} \times \mathbf{H}^{\text{eff}} + \frac{\alpha}{M_s} \mathbf{M} \times \partial_t \mathbf{M}, \quad (\text{B1})$$

where γ is the gyromagnetic ratio, α is the Gilbert damping constant, and M_s is the saturation magnetization. The effective magnetic field is defined via the functional derivative of the free-energy density U ,

$$\mathbf{H}^{\text{eff}} = -\frac{1}{\mu_0} \frac{\partial U}{\partial \mathbf{M}}. \quad (\text{B2})$$

The total magnetic energy density in the ferromagnetic layer consists of several contributions. The Zeeman energy density is

$$U^Z = -\mu_0 \mathbf{H} \cdot \mathbf{M}, \quad (\text{B3})$$

and the demagnetization energy density is

$$U^{\text{dm}} = \frac{1}{2} \mu_0 \mathbf{M} \cdot \mathbf{N} \cdot \mathbf{M}, \quad (\text{B4})$$

where \mathbf{N} denotes the demagnetization tensor. The magnetoelastic energy density is written as

$$U^{\text{me}} = \frac{1}{M_s^2} \sum_{ij} M_i M_j [B_{ij} \varepsilon_{ij} + K_{ij} \omega_{ij}], \quad (\text{B5})$$

where ε_{ij} is the strain tensor and ω_{ij} is the rotation tensor. The magnetoelastic coefficients are parameterized as $B_{ij} = \delta_{ij} B_{\parallel} + (1 - \delta_{ij}) B_{\perp}$ with B_{\parallel} and B_{\perp} being the

longitudinal and transverse magnetoelastic constants, respectively [92]. The magnetorotation coupling K_{ij} originates from the rotation of the hard anisotropy axis.

The elastic free-energy density of the non-magnetic substrate is given by

$$U^{\text{el}} = \sum_{ijpq} \frac{\rho}{2} (\partial_t u_i)^2 + \frac{\varepsilon_{ij} c_{ijpq} \varepsilon_{pq}}{2}, \quad (\text{B6})$$

where ρ is the mass density, c_{ijpq} is the fourth-rank stiffness tensor, and the indices i, j, p, q run over Cartesian coordinates. The elastic energy density of the ferromagnetic layer has the same structure, with the corresponding stiffness tensor and mass density denoted by tilted quantities.

To obtain the magnetic susceptibility, we expand the magnetic energy density up to quadratic order in the transverse components, using $M_z = M_s [1 - (M_x^2 + M_y^2) / 2M_s^2]$. We introduce circular variables $M_{\pm} = \frac{1}{\sqrt{2}} (M_x \mp iM_y)$, $H_{\pm} = \frac{1}{\sqrt{2}} (H_x \mp iH_y)$. For an external magnetic field $\mu_0 H_0$ applied perpendicular to the film plane (out-of-plane geometry), the magnetic susceptibility with respect to right-circularly polarized field reads

$$\chi^{\text{oop}} = \frac{\omega_{\text{M}_{\text{eff}}}^{\text{oop}}}{\omega_{\text{H}} - \omega_{\text{M}_{\text{eff}}}^{\text{oop}} - i\kappa_s - g^{\text{me}} - \omega}, \quad (\text{B7})$$

For an external magnetic field applied in the film plane (in-plane geometry), the susceptibility becomes

$$\chi^{\text{ip}} = \frac{\omega_{\text{M}_{\text{eff}}}^{\text{ip}}}{(\omega_{\text{H}} - i\kappa_s) \left(\omega_{\text{H}} + \omega_{\text{M}_{\text{eff}}}^{\text{ip}} - i\kappa_s - g^{\text{me}} \right) - \omega^2} \left(\omega_{\text{H}} + \frac{\omega_{\text{M}_{\text{eff}}}^{\text{ip}}}{2} - i\kappa_s - \frac{g^{\text{me}}}{2} - \omega \right). \quad (\text{B8})$$

Here we introduced $\omega_{\text{M}_{\text{eff}}^{\text{op,ip}}} = \gamma\mu_0 M_{\text{eff}}^{\text{op,ip}}$, $\omega_{\text{H}} = \gamma\mu_0 H_{\text{ext}}$, the magnetic damping rate κ_s and the magnetoelastic parameter

$$g^{\text{me}} = \frac{\gamma}{M_{\text{eff}}^{\text{op,ip}}} \left(B_{\perp} + \frac{\mu_0 (M_{\text{eff}}^{\text{op,ip}})^2}{2} \right)^2 \frac{C_{4,4} k \sin(kL) \sin(\tilde{k}d) + 4\tilde{C}_{4,4} \tilde{k} \cos(kL) \sin^2(\tilde{k}d/2)}{\tilde{C}_{4,4} \tilde{k} d [C_{4,4} k \sin(kL) \cos(\tilde{k}d) + \tilde{C}_{4,4} \tilde{k} \cos(kL) \sin(\tilde{k}d)]}. \quad (\text{B9})$$

The wave number of transverse elastic waves in the ferromagnetic layer is

$$\tilde{k} = \sqrt{\frac{\omega^2}{\tilde{v}_t^2} + i \frac{2\tilde{\eta}_a \omega}{\tilde{v}_t^2}}, \quad (\text{B10})$$

while in the non-magnetic substrate it is

$$k = \sqrt{\frac{\omega^2}{v_t^2} + i \frac{2\eta_a \omega}{v_t^2}}. \quad (\text{B11})$$

Here c_t and \tilde{c}_t are the transverse sound velocities in the substrate and ferromagnet, respectively, and η_a and $\tilde{\eta}_a$ denote the corresponding elastic damping coefficients. The stiffness components C_{44} and \tilde{C}_{44} are expressed in Voigt notation.

REFERENCES

- ¹M. Weiler, L. Dreher, C. Heeg, H. Huebl, R. Gross, M. S. Brandt, and S. T. B. Goennenwein, "Elastically Driven Ferromagnetic Resonance in Nickel Thin Films," *Phys. Rev. Lett.* **106**, 117601 (2011).
- ²M. Weiler, H. Huebl, F. S. Goerg, F. D. Czeschka, R. Gross, and S. T. B. Goennenwein, "Spin Pumping with Coherent Elastic Waves," *Phys. Rev. Lett.* **108**, 176601 (2012).
- ³P. G. Gowtham, G. M. Stiehl, D. C. Ralph, and R. A. Buhrman, "Thickness-dependent magnetoelasticity and its effects on perpendicular magnetic anisotropy in Ta/CoFeB/MgO thin films," *Phys. Rev. B* **93**, 024404 (2016).
- ⁴M. Küß, M. Heigl, L. Flacke, A. Hörner, M. Weiler, M. Albrecht, and A. Wixforth, "Nonreciprocal Dzyaloshinskii-Moriya Magnetoacoustic Waves," *Phys. Rev. Lett.* **125**, 217203 (2020).
- ⁵M. Küß, M. Heigl, L. Flacke, A. Hefele, A. Hörner, M. Weiler, M. Albrecht, and A. Wixforth, "Symmetry of the Magnetoelastic Interaction of Rayleigh and Shear Horizontal Magnetoacoustic Waves in Nickel Thin Films on LiTaO₃," *Phys. Rev. Appl.* **15**, 034046 (2021).
- ⁶M. Küß, M. Heigl, L. Flacke, A. Hörner, M. Weiler, A. Wixforth, and M. Albrecht, "Nonreciprocal Magnetoacoustic Waves in Dipolar-Coupled Ferromagnetic Bilayers," *Phys. Rev. Appl.* **15**, 034060 (2021).
- ⁷T. Kikkawa, K. Shen, B. Flebus, R. A. Duine, K.-i. Uchida, Z. Qiu, G. E. Bauer, and E. Saitoh, "Magnon Polarons in the Spin Seebeck Effect," *Phys. Rev. Lett.* **117**, 207203 (2016).
- ⁸Y. Hashimoto, T. H. Johansen, and E. Saitoh, "180°-Phase Shift of Magnetoelastic Waves Observed By Phase-Resolved Spin-Wave Tomography," *Appl. Phys. Lett.* **112** (2018).
- ⁹X. Zhang, A. Galda, X. Han, D. Jin, and V. M. Vinokur, "Broadband Nonreciprocity Enabled by Strong Coupling of Magnons and Microwave Photons," *Phys. Rev. Appl.* **13**, 044039 (2020).
- ¹⁰D. Hatanaka, M. Asano, H. Okamoto, Y. Kunihashi, H. Sanada, and H. Yamaguchi, "On-Chip Coherent Transduction between Magnons and Acoustic Phonons in Cavity Magnomechanics," *Phys. Rev. Appl.* **17**, 034024 (2022).
- ¹¹K. Künstle, Y. Kunz, T. Moussa, K. Lasinger, K. Yamamoto, P. Pirro, J. F. Gregg, A. Kamra, and M. Weiler, "Magnon-polaron control in a surface magnetoacoustic wave resonator,"

- Nat. Commun.* **16**, 10116 (2025).
- ¹²E. G. Spencer and R. C. LeCraw, "Magnetoacoustic Resonance in Yttrium Iron Garnet," *Phys. Rev. Lett.* **1**, 241–243 (1958).
 - ¹³A. Widom, C. Vittoria, and S. D. Yoon, "Gilbert ferromagnetic damping theory and the fluctuation-dissipation theorem," *Journ. Appl. Phys.* **108**, 073924 (2010).
 - ¹⁴C. Vittoria, S. D. Yoon, and A. Widom, "Relaxation mechanism for ordered magnetic materials," *Phys. Rev. B* **81**, 014412 (2010).
 - ¹⁵E. Rossi, O. G. Heinonen, and A. H. MacDonald, "Dynamics of magnetization coupled to a thermal bath of elastic modes," *Phys. Rev. B* **72**, 174412 (2005).
 - ¹⁶T. Kobayashi, R. C. Barker, and A. Yelon, "Ferromagnetoelastic Resonance in Thin Films. II. Application to Nickel," *Phys. Rev. B* **7**, 3286–3297 (1973).
 - ¹⁷T. Kobayashi, R. C. Barker, J. L. Bleustein, and A. Yelon, "Ferromagnetoelastic Resonance in Thin Films. I. Formal Treatment," *Phys. Rev. B* **7**, 3273–3285 (1973).
 - ¹⁸M. Weiler, A. Brandlmaier, S. Geprägs, M. Althammer, M. Opel, C. Bihler, H. Huebl, M. S. Brandt, R. Gross, and S. T. B. Goennenwein, "Voltage controlled inversion of magnetic anisotropy in a ferromagnetic thin film at room temperature," *New J. Phys.* **11**, 013021 (2009).
 - ¹⁹K. Uchida, H. Adachi, T. An, T. Ota, M. Toda, B. Hillebrands, S. Maekawa, and E. Saitoh, "Long-range spin Seebeck effect and acoustic spin pumping," *Nat. Mater.* **10**, 737–741 (2011).
 - ²⁰L. Thevenard, C. Gourdon, J. Y. Prieur, H. J. von Bardeleben, S. Vincent, L. Becerra, L. Largeau, and J.-Y. Duquesne, "Surface-acoustic-wave-driven ferromagnetic resonance in (Ga,Mn)(As,P) epilayers," *Phys. Rev. B* **90**, 094401 (2014).
 - ²¹L. Thevenard, J.-Y. Duquesne, E. Peronne, H. J. von Bardeleben, H. Jaffres, S. Ruttala, J.-M. George, A. Lemaitre, and C. Gourdon, "Irreversible magnetization switching using surface acoustic waves," *Phys. Rev. B* **87**, 144402 (2013).
 - ²²S. Geprägs, A. Brandlmaier, M. Opel, R. Gross, and S. T. B. Goennenwein, "Electric field controlled manipulation of the magnetization in Ni/BaTiO₃ hybrid structures," *Appl. Phys. Lett.* **96**, 142509 (2010).
 - ²³S. Geprägs, A. Brandlmaier, M. Brandt, R. Gross, and S. Goennenwein, "Strain-controlled nonvolatile magnetization switchin," *Solid State Commun.* **198**, 7–12 (2014), sI: Spin Mechanics.
 - ²⁴A. Brandlmaier, S. Geprägs, M. Weiler, A. Boger, M. Opel, H. Huebl, C. Bihler, M. S. Brandt, B. Botters, D. Grundler, R. Gross, and S. T. B. Goennenwein, "In situ manipulation of magnetic anisotropy in magnetite thin films," *Phys. Rev. B* **77**, 104445 (2008).
 - ²⁵L. Dreher, M. Weiler, M. Pernpeintner, H. Huebl, R. Gross, M. S. Brandt, and S. T. B. Goennenwein, "Surface acoustic wave driven ferromagnetic resonance in nickel thin films: Theory and experiment," *Phys. Rev. B* **86**, 134415 (2012).
 - ²⁶Q. ul ain, D. Odkhuu, S. H. Rhim, and S. C. Hong, .
 - ²⁷L. Bi, H.-S. Kim, G. F. Dionne, and C. A. Ross, "Structure, magnetic properties and magnetoelastic anisotropy in epitaxial Sr(Ti_{1-x}Co_x)O₃ films," *New J. Phys.* **12**, 043044 (2010).
 - ²⁸K. An, X. Ma, C.-F. Pai, J. Yang, K. S. Olsson, J. L. Erskine, D. C. Ralph, R. A. Buhrman, and X. Li, "Current control of magnetic anisotropy via stress in a ferromagnetic metal waveguide," *Phys. Rev. B* **93**, 140404 (2016).
 - ²⁹R. Yahiro, T. Kikkawa, R. Ramos, K. Oyanagi, T. Hioki, S. Daimon, and E. Saitoh, "Magnon polarons in the spin Peltier effect," *Phys. Rev. B* **101**, 024407 (2020).
 - ³⁰A. S. Sukhanov, M. S. Pavlovskii, P. Bourges, H. C. Walker, K. Manna, C. Felser, and D. S. Inosov, "Magnon-polaron excitations in the noncollinear antiferromagnet Mn₃Ge," *Phys. Rev. B* **99**, 214445 (2019).
 - ³¹H. Hayashi and K. Ando, "Spin Pumping Driven by Magnon Polarons," *Phys. Rev. Lett.* **121**, 237202 (2018).
 - ³²A. Brataas, B. van Wees, O. Klein, G. de Loubens, and M. Viret, "Spin insulatronics," *Phys. Rep.* **885**, 1–27 (2020).
 - ³³S. Streib, H. Keshtgar, and G. E. Bauer, "Damping of Magnetization Dynamics by Phonon Pumping," *Phys. Rev. Lett.* **121**, 027202 (2018).
 - ³⁴T. Sato, W. Yu, S. Streib, and G. E. W. Bauer, "Dynamic magnetoelastic boundary conditions and the pumping of phonons," *Phys. Rev. B* **104**, 014403 (2021).
 - ³⁵K. An, A. N. Litvinenko, R. Kohno, A. A. Fuad, V. V. Naletov, L. Vila, U. Ebels, G. de Loubens, H. Hurdequint, N. Beaulieu, J. Ben Youssef, N. Vukadinovic, G. E. W. Bauer, A. N. Slavin, V. S. Tiberkevich, and O. Klein, "Coherent long-range transfer of angular momentum between magnon Kittel modes by phonons," *Phys. Rev. B* **101**, 060407 (2020).
 - ³⁶K. An, R. Kohno, A. N. Litvinenko, R. L. Seeger, V. V. Naletov, L. Vila, G. de Loubens, J. Ben Youssef, N. Vukadinovic, G. E. W. Bauer, A. N. Slavin, V. S. Tiberkevich, and O. Klein, "Bright and Dark States of Two Distant Macrosppins Strongly Coupled by Phonons," *Phys. Rev. X* **12**, 011060 (2022).
 - ³⁷R. Schlitz, L. Siegl, T. Sato, W. Yu, G. E. W. Bauer, H. Huebl, and S. T. B. Goennenwein, "Magnetization dynamics affected by phonon pumping," *Phys. Rev. B* **106**, 014407 (2022).
 - ³⁸S. Sharma, V. S V Bittencourt, and S. Viola Kusminskiy, "Protocol for generating an arbitrary quantum state of the magnetization in cavity magnonics," *J. Phys. Mater* **5**, 034006 (2022).
 - ³⁹V. A. S. V. Bittencourt, I. Liberal, and S. Viola Kusminskiy, "Optomagnonics in Dispersive Media: Magnon-Photon Coupling Enhancement at the Epsilon-near-Zero Frequency," *Phys. Rev. Lett.* **128**, 183603 (2022).
 - ⁴⁰V. Wachter, V. A. S. V. Bittencourt, S. Xie, S. Sharma, N. Joly, P. S. Russell, F. Marquardt, and S. V. Kusminskiy, "Optical signatures of the coupled spin-mechanics of a levitated magnetic microparticle," *J. Opt. Soc. Am. B* **38**, 3858–3871 (2021).
 - ⁴¹C. A. Potts, E. Varga, V. A. S. V. Bittencourt, S. V. Kusminskiy, and J. P. Davis, "Dynamical Backaction Magnomechanics," *Phys. Rev. X* **11**, 031053 (2021).
 - ⁴²K. An, C. Kim, K.-W. Moon, R. Kohno, G. Olivetti, G. de Loubens, N. Vukadinovic, J. Ben Youssef, C. Hwang, and O. Klein, "Optimizing the Magnon-Phonon Cooperativity in Planar Geometries," *Phys. Rev. Appl.* **20**, 014046 (2023).
 - ⁴³H. Keshtgar, M. Zareyan, and G. E. Bauer, "Acoustic parametric pumping of spin waves," *Solid State Commun.* **198**, 30–34 (2014).
 - ⁴⁴B. Flebus, K. Shen, T. Kikkawa, K.-i. Uchida, Z. Qiu, E. Saitoh, R. A. Duine, and G. E. W. Bauer, "Magnon-polaron transport in magnetic insulators," *Phys. Rev. B* **95**, 144420 (2017).
 - ⁴⁵S. Sharma, V. S V Bittencourt, and S. Viola Kusminskiy, "Protocol for generating an arbitrary quantum state of the magnetization in cavity magnonics," *JPhys Materials* **5**, 034006 (2022).
 - ⁴⁶J. Graf, S. Sharma, H. Huebl, and S. V. Kusminskiy, "Design of an optomagnonic crystal: Towards optimal magnon-photon mode matching at the microscale," *Phys. Rev. Res.* **3**, 013277 (2021).
 - ⁴⁷F. Engelhardt, V. Bittencourt, H. Huebl, O. Klein, and S. V. Kusminskiy, "Optimal Broadband Frequency Conversion via a Magnetomechanical Transducer," *Phys. Rev. Appl.* **18**, 044059 (2022).
 - ⁴⁸S. Kim, B. Sharif, S. Dhuey, T. D. Yuzvinsky, W. Yang, D. Ledorman, and H. Schmidt, "Engineering strong magnon-phonon coupling in single CoFe nanomagnets," *Journ. Appl. Phys.* **137**, 123904 (2025).
 - ⁴⁹R.-C. Shen, J. Li, Y.-M. Sun, W.-J. Wu, X. Zuo, Y.-P. Wang, S.-Y. Zhu, and J. Q. You, "Cavity-Magnon Polaritons Strongly Coupled to Phonons," *Nat. Commun.* **16**, 5652 (2025).
 - ⁵⁰J. Cui, E. V. Boström, M. Ozerov, F. Wu, Q. Jiang, J.-H. Chu, C. Li, F. Liu, X. Xu, A. Rubio, and Q. Zhang, "Chirality Selective Magnon-Phonon Hybridization and Magnon-Induced Chiral Phonons in a Layered Zigzag Antiferromagnet," *Nat. Commun.* **14**, 3396 (2023).
 - ⁵¹H. Matsumoto, I. Yasuda, M. Asano, Y. Todaka, T. Kawada, M. Kawaguchi, D. Hatanaka, and M. Hayashi, "Magnon-Phonon Coupling of Synthetic Antiferromagnets in a Surface Acoustic Wave Cavity Resonator," *Nano Lett.* **24**, 5683–5689 (2024).
 - ⁵²H. Maier-Flaig, S. Klingler, C. Dubs, O. Surzhenko, R. Gross,

- M. Weiler, H. Huebl, and S. T. B. Goennenwein, "Temperature-dependent magnetic damping of yttrium iron garnet spheres," *Phys. Rev. B* **95**, 214423 (2017).
- ⁵³C. L. Jermain, S. V. Aradhya, N. D. Reynolds, R. A. Buhman, J. T. Brangham, M. R. Page, P. C. Hammel, F. Y. Yang, and D. C. Ralph, "Increased low-temperature damping in yttrium iron garnet thin films," *Phys. Rev. B* **95**, 174411 (2017).
- ⁵⁴E. G. Spencer, R. C. LeCraw, and A. M. Clogston, "Low-Temperature Line-Width Maximum in Yttrium Iron Garnet," *Phys. Rev. Lett.* **3**, 32–33 (1959).
- ⁵⁵S. Klingler, H. Maier-Flaig, C. Dubs, O. Surzhenko, R. Gross, H. Huebl, S. T. B. Goennenwein, and M. Weiler, "Gilbert damping of magnetostatic modes in a yttrium iron garnet sphere," *Appl. Phys. Lett.* **110**, 092409 (2017).
- ⁵⁶D. Lachance-Quirion, Y. Tabuchi, A. Gloppe, K. Usami, and Y. Nakamura, "Hybrid quantum systems based on magnonics," *Appl. Phys. Express* **12**, 070101 (2019).
- ⁵⁷R. O. Serha, A. A. Voronov, D. Schmoll, R. Klingbeil, S. Knauer, S. Koraltan, E. Pribytova, M. Lindner, T. Reimann, C. Dubs, C. Abert, R. Verba, M. Urbánek, D. Suess, and A. V. Chumak, "Damping enhancement in YIG at millikelvin temperatures due to GGG substrate," *Materials Today Quantum* **5**, 100025 (2025).
- ⁵⁸J. de Klerk, "Behavior of Coherent Microwave Phonons at Low Temperatures in Al_2O_3 using Vapor-Deposited Thin-Film Piezoelectric Transducers," *Phys. Rev.* **139**, A1635–A1639 (1965).
- ⁵⁹"28 - On the absorption of sound in solids," in *Collected Papers of L.D. Landau*, edited by D. ter Haar (Pergamon, 1965) pp. 187–192.
- ⁶⁰M. Müller, J. Weber, F. Engelhardt, V. A. S. V. Bittencourt, T. Luschmann, M. Cherkasskii, M. Opel, S. T. B. Goennenwein, S. Viola Kusminskiy, S. Geprägs, R. Gross, M. Althammer, and H. Huebl, "Chiral phonons and phononic birefringence in ferromagnetic metal–bulk acoustic resonator hybrids," *Phys. Rev. B* **109**, 024430 (2024).
- ⁶¹M. Müller, J. Weber, S. Goennenwein, S. V. Kusminskiy, R. Gross, M. Althammer, and H. Huebl, "Temperature dependence of the magnon-phonon interaction in hybrids of high-overtone bulk acoustic resonators with ferromagnetic thin films," *Phys. Rev. Appl.* **21**, 034032 (2024).
- ⁶²E. R. Callen, A. E. Clark, B. DeSavage, W. Coleman, and H. B. Callen, "Magnetostriction in Cubic Néel Ferrimagnets, with Application to YIG," *Phys. Rev.* **130**, 1735–1740 (1963).
- ⁶³P. Hansen, K. Enke, and G. Winkler, "A. Rare-earth garnets of composition $\text{Y}_{3-x}\text{R}_x\text{Fe}_5\text{O}_{12}$," in *Part A: Garnets and Perovskites* (Springer-Verlag, Berlin/Heidelberg) pp. 156–159.
- ⁶⁴M. Barangi and P. Mazumder, "Effect of temperature variations and thermal noise on the static and dynamic behavior of straintronics devices," *Journ. Appl. Phys.* **118**, 173902 (2015).
- ⁶⁵H. Maier-Flaig, S. T. B. Goennenwein, R. Ohshima, M. Shiraishi, R. Gross, H. Huebl, and M. Weiler, "Note: Derivative divide, a method for the analysis of broadband ferromagnetic resonance in the frequency domain," *Rev. Sci. Instrum.* **89**, 076101 (2018).
- ⁶⁶We experimentally determine S_{21}^0 by measuring the complex transmission parameter S_{21} far off-resonant with the FMR mode.
- ⁶⁷G. Dionne, *Magnetic Oxides* (Springer US, 2014).
- ⁶⁸X. Zhang, C.-L. Zou, L. Jiang, and H. X. Tang, "Strongly Coupled Magnons and Cavity Microwave Photons," *Phys. Rev. Lett.* **113**, 156401 (2014).
- ⁶⁹M. Cherkasskii, F. Engelhardt, M. Müller, J. Weber, M. Althammer, S. T. B. Goennenwein, H. Huebl, and S. Viola Kusminskiy, "Theory of polarization-dependent phonon pumping in ferromagnetic/non-magnetic bilayers," *Journ. Appl. Phys.* **138**, 043906 (2025).
- ⁷⁰A. Rückriegel, P. Kopietz, D. A. Bozhko, A. A. Serga, and B. Hillebrands, "Magnetoelastic modes and lifetime of magnons in thin yttrium iron garnet films," *Phys. Rev. B* **89**, 184413 (2014).
- ⁷¹A. Gurevich and G. Melkov, *Magnetization Oscillations and Waves* (CRC Press, 2020).
- ⁷²M. A. W. Schoen, J. M. Shaw, H. T. Nembach, M. Weiler, and T. J. Silva, "Radiative damping in waveguide-based ferromagnetic resonance measured via analysis of perpendicular standing spin waves in sputtered permalloy films," *Phys. Rev. B* **92**, 184417 (2015).
- ⁷³Since we are evaluating the data in a small frequency window, we assume that E is constant.
- ⁷⁴In our experiment, the surface normal on the YIG film is not perfectly aligned with the [111]-direction of the YIG and GGG crystal due to the presence of a small, but finite miscut of 0.003° . Ref. [69] as well as the adaption for the magnetic field aligned in-plane accounts for the resulting lifting in the degeneracy of the propagation velocities by distinguishing two shear wave velocities $v_{t,x}$ and $v_{t,y}$ with a velocity difference $v_{t,x} - v_{t,y} = \Delta v$.
- ⁷⁵Z. Kleszczewski and J. Bodzenta, "Phonon–Phonon Interaction in Gadolinium–Gallium Garnet Crystals," *Phys. Status Solidi B* **146**, 467–474 (1988).
- ⁷⁶D. Polder, "On the theory of ferromagnetic resonance," *Physica* **15**, 253–255 (1949).
- ⁷⁷G. Woltersdorf, M. Kiessling, G. Meyer, J.-U. Thiele, and C. H. Back, "Damping by Slow Relaxing Rare Earth Impurities in $\text{Ni}_{80}\text{Fe}_{20}$," *Phys. Rev. Lett.* **102**, 257602 (2009).
- ⁷⁸J. P. Wolfe, *Imaging Phonons* (Cambridge University Press, 1998).
- ⁷⁹R. L. Comstock and W. G. Nilsen, "Parallel pumping of magnetoelastic waves in lithium ferrite," *Phys. Rev.* **136**, A442–A445 (1964).
- ⁸⁰D. Fritsch and C. Ederer, "First-principles calculation of magnetoelastic coefficients and magnetostriction in the spinel ferrites CoFe_2O_4 and NiFe_2O_4 ," *Phys. Rev. B* **86**, 014406 (2012).
- ⁸¹C. Robert, "Nuclear Magnetic Resonance of Iron-57 Nuclei in Local Fields in Yttrium and Iron Garnets," Tech. Rep. (France. Commissariat a l'Energie Atomique. Centre d'Etudes Nucleaires, Saclay, 1961).
- ⁸²Ye, M., Brockmeyer, A., Wigen, P. E., and Dötsch, H., "Magnetoelastic resonances in epitaxial garnet films," *J. Phys. Colloques* **49**, C8–989–C8–990 (1988).
- ⁸³Note, that the coupling rate is defined so that frequency difference between the normal modes is $2g_{\text{eff}}$, which is in contrast to the definition used by An *et al* [42].
- ⁸⁴R. O. Serha, A. A. Voronov, D. Schmoll, R. Verba, K. O. Levchenko, S. Koraltan, K. Davidková, B. Budinská, Q. Wang, O. V. Dobrovolskiy, M. Urbánek, M. Lindner, T. Reimann, C. Dubs, C. Gonzalez-Ballester, C. Abert, D. Suess, D. A. Bozhko, S. Knauer, and A. V. Chumak, "Magnetic anisotropy and ggg substrate stray field in yig films down to millikelvin temperatures," *npj Spintronics* **2**, 29 (2024).
- ⁸⁵A. Rashedi, M. Ebrahimi, Y. Huang, M. Rudd, J. Davis, and V. Bittencourt, "Photonic crystal cavities based on suspended yttrium iron garnet nanobeams," *Phys. Rev. Appl.* **24**, 054017 (2025).
- ⁸⁶C. Kittel, "On the Theory of Ferromagnetic Resonance Absorption," *Phys. Rev.* **73**, 155–161 (1948).
- ⁸⁷O. Kohmoto, "Effective demagnetizing factors in ferromagnetic resonance equations," *Journal of Magnetism and Magnetic Materials* **262**, 280–288 (2003).
- ⁸⁸S. Lee, S. Grudichak, J. Sklenar, C. C. Tsai, M. Jang, Q. Yang, H. Zhang, and J. B. Ketterson, "Ferromagnetic resonance of a YIG film in the low frequency regime," *Journ. Appl. Phys.* **120**, 033905 (2016).
- ⁸⁹C. Dubs, O. Surzhenko, R. Thomas, J. Osten, T. Schneider, K. Lenz, J. Grenzer, R. Hübner, and E. Wendler, "Low damping and microstructural perfection of sub-40nm-thin yttrium iron garnet films grown by liquid phase epitaxy," *Phys. Rev. Mater.* **4**, 024416 (2020).
- ⁹⁰F. Bloch, "Zur Theorie des Ferromagnetismus," *Z. Phys.* (1930).
- ⁹¹I. Boventer, M. Pfirmann, J. Krause, Y. Schön, M. Kläui, and M. Weides, "Complex temperature dependence of coupling and dissipation of cavity magnon polaritons from millikelvin to room temperature," *Phys. Rev. B* **97**, 184420 (2018).

⁹²In the main part the transverse magnetoelastic parameters are denoted as B_{OOP} and B_{IP} .